Experiments in Fluids 37 (2004) 105–119
DOI 10.1007/s00348-004-0790-6

# Optically sliced micro-PIV using confocal laser scanning microscopy (CLSM)

**Jae Sung Park, Chang Kyoung Choi, Kenneth D. Kihm**



**Abstract** Optically sliced microscopic-particle image velocimetry (micro-PIV) is developed using confocal laser scanning microscopy (CLSM). The developed PIV system shows a unique optical slicing capability allowing true depth-wise resolved micro-PIV vector field mapping. A comparative study between CLSM micro-PIV and conventional epi-fluorescence micro-PIV is presented. Both techniques have been applied to the creeping Poiseuille flows in two different microtubes of 99-μm ($Re$=0.00275) and 516-μm ID diameters ($Re$=0.021), which are respectively imaged by a 40×-0.75$NA$ objective with an estimated 2.8-μm optical slice thickness, and by a 10×-0.30$NA$ objective with a 26.7-μm slicing. Compared to conventional micro-PIV, CLSM micro-PIV consistently shows significantly improved particle image contrasts, definitions, and measured flow vector fields agreeing more accurately with predictions based on the Poiseuille flow fields. The data improvement due to the optical slicing of CLSM micro-PIV is more pronounced with higher magnification imaging with higher $NA$ objectives for a smaller microtube.

## 1 Introduction

Confocal microscopy, patented by Minsky (1998) at Harvard University in 1957, dramatically improves optical resolutions in microscopic imaging to an unprecedented level of 180-nm lateral resolution and 500-nm axial resolution. The more important feature of the confocal microscopy is its ability to deliver extremely thin, in-focus images by true means of depth-wise optical slicing, and allowing the gathering of 3-D reconstructed information from the line-of-sight depth-wise resolved imaging without the need for physical slicing of specimens.

The basic "confocal" concept is described by point-scanning of the laser excitation and a spatially filtered fluorescence signal emitting from the focal point onto the confocal point (Fig. 1a). The pinhole aperture, located at the confocal point, exclusively allows the emitted fluorescent light from the focal point (solid rays) to pass through the detector, and filters out the fluorescent light emitted from outside of the focal point (dashed rays). This spatial filtering is the key principle to enhance the optical resolutions by devising depth-wise optical slicing. The illuminating laser can rapidly scan from point to point on a single focal plane, in a synchronized way with the aperture, to complete a full-field image on the detector (Fig. 1b). The scan is repeated for multiple focal planes to reconstruct 3-D images. The practice of confocal microscopy (Webb 1996) has been widely used in biology, materials study, and medical research, often associated with laser-induced fluorescence (LIF) imaging, to allow microstructures to be visible where they would be otherwise invisible or poorly visible.

Optical characterization of confocal microscopy has been fairly well studied by a number of optics researchers. The depth discrimination capability of this microscopy has been analytically characterized for a range of fluorescence wavelengths and the simulation results have been compared with the corresponding experimental results (Kimura and Munakata 1990). A quantitative theoretical analysis for standard confocal microscopy, in conjunction with 3-D fluorescence correlation spectroscopy, has been developed using a point-spread function in conjunction with a collection efficiency function (Qian and Elson 1991). Aberration compensations for confocal microscopy were discussed for spherical aberrations occurring when one is focusing deep within the specimen (Sheppard and Gu 1991), and for additional aberrations induced by mismatches in refractive index values across, or inside, the specimen (Hell et al. 1993). An extensive study by Sandison and Webb (1994) shows that the signal-to-background ratio, with background defined as the detected light originating from outside a resolution volume, obtained with a confocal microscope can be more than 100 times greater than the signal-to-background ratio available with a conventional microscope, and the optimized confocal signal-to-noise ratio can be a factor of ten greater than that of the conventional microscope.

*Received: 9 September 2003 / Accepted: 25 January 2004*
*Published online: 19 March 2004*


J. S. Park, C. K. Choi, K. D. Kihm (✉)
Micro/Nano-scale Fluidics and Heat Transport Laboratory,
Department of Mechanical Engineering, Texas A&M University,
College Station, Texas 77843–3123, USA
E-mail: ken-kihm@tamu.edu
Tel.: +1-979-8452143

The confocal laser scanning microscope (CLSM) system was purchased by the Texas A&M Permanent University Facility (PUF) Award granted to Dr. Kihm's Micro/nano-scale Fluidics and Heat Transport Laboratory http://go.to/microlab. The authors acknowledge that the current research has been partially sponsored by the NASA-Fluid Physics Research Program, grant no. NAG 3–2712, and partially by a subcontract from the R4D Program at the National Center for Microgravity Research (NCMR). The presented technical contents are not necessarily the representative views of NASA or NCMR.

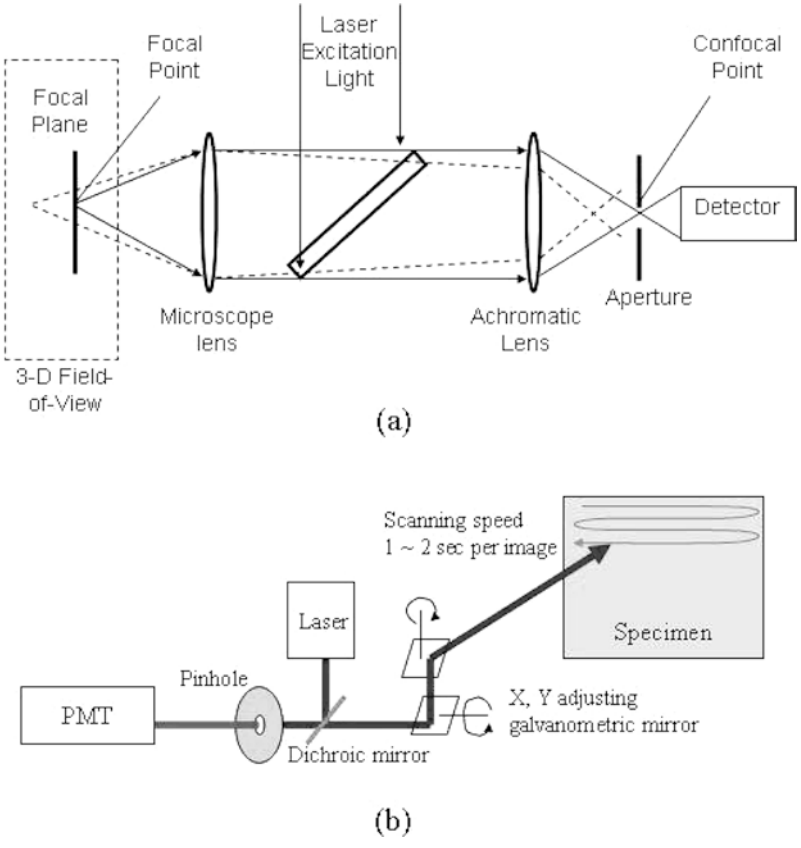


**Fig. 1a, b.** Principle of confocal microscopy using a pinhole as a spatial filter (**a**) and a schematic illustration of galvanometric scanning to conform to a full-field image (**b**)

As shown in Fig. 1b, the galvanometric steering of the focal point of traditional confocal microscopy limits its scanning speed to approximately one frame-per-second (FPS), which is too slow for real-time observation of moving objects at any practical speed. The innovative use of a rotating micro-lens array (Conchello and Lichtman 1994; Tiziani and Uhda 1994) replacing the single pinhole makes it possible for confocal microscopy to scan full-field images at substantially higher FPS rates. Further study has been carried out on performing high-speed confocal microscopy by using a rotating scanner for advanced bio-medical applications of real-time 3-D imaging of single molecular fluorescence (Ichihara et al. 1996). Both theoretical and experimental comparisons have been studied for the depth-wise resolution of high-speed confocal microscopy with multifocal and multiphoton microscopy (Egner et al. 2002).

The essential innovation of confocal laser scanning microscopy (CLSM, http://www.solameretech.com) is the use of dual high-speed spinning disks, as shown in Fig. 2; the upper disk is a rotating scanner that consists of 20,000

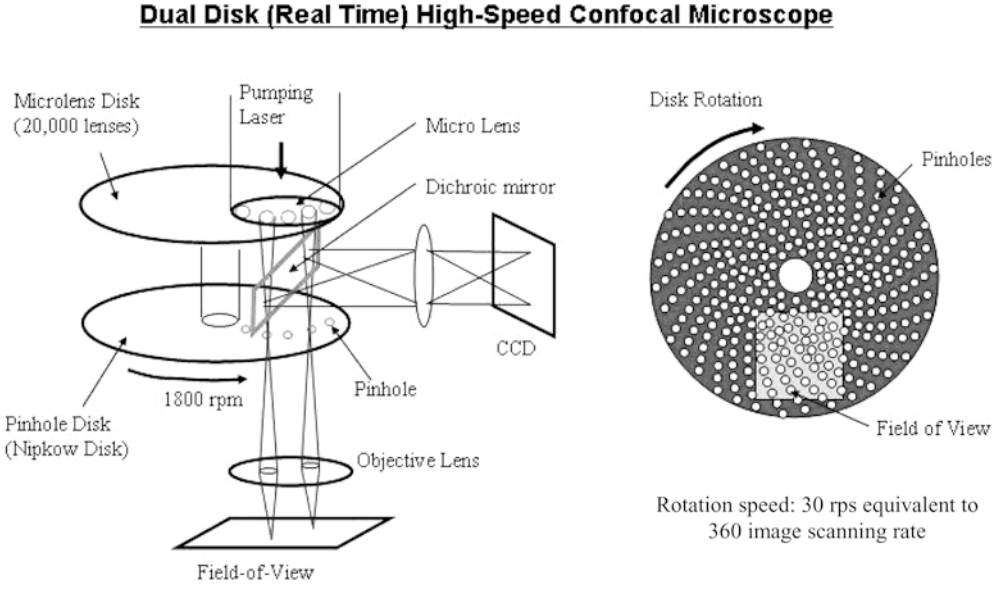


**Fig. 2.** Principle of dual-Nipkow disk design for high-speed confocal laser scanning microscopy (CLSM)

**Table 1.** Lateral/axial resolution and optical slice thickness for both conventional and confocal microscope systems (Webb 1996; Wilhelm et al. 2003; http://www.health.auckland.ac.nz/biru/confocal_microscopy; http://www.microscopy.fsu.edu)

| | | Conventional microscope | Geometric-optical confocal microscope | Wave-optical confocal microscope |
|---|---|---|---|---|
| Lateral resolution | | $\frac{0.61\lambda_{em}}{NA}$ | $\frac{0.51\lambda_{ex}}{NA}$ | $\frac{0.37\bar{\lambda}}{NA}$ |
| Axial resolution | $NA \geq 0.5$ | $2\frac{n\cdot\lambda_{em}}{NA^2}$ | $\frac{0.88\lambda_{ex}}{n-\sqrt{n^2-NA^2}}$ | $\frac{0.64\bar{\lambda}}{n-\sqrt{n^2-NA^2}}$ |
| | $NA < 0.5$ | | $\frac{1.67n\cdot\lambda_{ex}}{NA^2}$ | $\frac{1.28n\cdot\bar{\lambda}}{NA^2}$ |
| Optical slice thickness | | No definition | $\sqrt{\left(\frac{0.88\lambda_{em}}{n-\sqrt{n^2-NA^2}}\right)^2+\left(\frac{\sqrt{2}n\cdot PD}{NA}\right)^2}$ | $\frac{0.64\bar{\lambda}}{n-\sqrt{n^2-NA^2}}$ |



micro-lenses, and the lower one is called a Nipkow disk that consists of 20,000 matching pinholes of 50 μm in diameter. Both the incident excitation light and emitting fluorescence light paths are defined by a similar optical path. The pumping light is focused by the micro-lenses of the scanning disk through the pinholes on the Nipkow disk. A dichroic mirror, located between the two disks, reflects the returning confocal fluorescence image to the CCD for real-time, true-color recording. As the disk has a rotation speed of 30 RPS with a possible scan rate of 360 per second, and together with the fact that the multiple pinholes sweep the view, full-field imaging of up to 120 FPS is achieved by averaging three sweeps per single field for statistical enhancement.

The idea is that CLSM can accommodate the use of particle image velocimetry (Raffel et al. 1998) to provide optically sliced micro-fluidic velocity field mapping. To date (to the authors' knowledge), the use of CLSM for micro-PIV has not been published in open literature. Characterization of CLSM micro-PIV, in comparison with conventional micro-PIV (Santiago et al. 1998; Sugii et al. 2002), is presented by measuring the same flow configurations under otherwise identical optical conditions of image magnification, field illumination, and fluorescence filtering. Detailed flow measurements have been conducted for Poiseuille flows developed in microtubes of nominal 100-μm and 500-μm internal diameters (ID), and comparative results are presented between CLSM micro-PIV and conventional epi-fluorescence micro-PIV results.

## 2
## Lateral/axial image resolution and optical image slicing

### 2.1
### Conventional microscope

When the Fraunhofer condition[1] is satisfied, microscopic particle imaging can be depicted by the Fraunhofer diffraction rings, called the Airy function (Hecht 2002). Two neighboring objects are said to be marginally resolved when the center of one Airy disk falls on the first minimum of the other Airy pattern, i.e., the so-called Rayleigh criterion for monochromatic imaging. The Rayleigh criterion is generally defined as the lateral resolution for conventional microscopic imaging and is used to estimate the minimum resolvable distance between two point sources of light generated from a specimen. If the emitted wavelengths, $\lambda_{em}$, of point sources are all the same, then their Airy disks have the same diameter, as long as they are constructed by the same objective with a specified $NA$[2]. Thus, the Rayleigh criterion is equal to the radius of the Airy disk, i.e., $0.61\lambda_{em}/NA$, where $NA$ is the numerical aperture of the microscopic objective lens, as summarized with other relevant formulae in Table 1.

Unlike the lateral Fraunhofer diffraction, the axial diffraction pattern of a point source does not constitute a disk shape but an hourglass shape or flare of the point spread function (PSF). A similar reasoning can be used to draw the axial Rayleigh criterion (Webb 1996), which is defined by taking the distance from the maximum intensity location at the focal plane to the first location of the minimum intensity along the optical axis, or equivalently, $2\frac{n\cdot\lambda_{em}}{NA^2}$ (from Table 1). Note that the axial resolution increases with increasing refractive index of the medium, $n$, whereas the lateral resolution is independent of $n$. In the usual sense, the depth-of-field (DOF) is referred to as the defocusing range from the focal plane image of a single particle or object before it blurs "unacceptably", and is conventionally defined as one-half of the axial resolution, i.e., $\mathrm{DOF} \equiv \frac{n\cdot\lambda_{em}}{NA^2}$.

When imaging is conducted for multiple particles existing in the line-of-sight direction like most cases of PIV imaging, however, the DOF can be misleading since it does not constitute the true meaning of depth-wise optical slicing, and the resulting images are inevitably obscured by blurred images from both the foreground and background. The signal-to-noise ratio of conventional microscopy, which was defined as the ratio of the focused image intensity to the average background intensity, was extensively studied in terms of a test section depth and a particle concentration (Meinhart et al. 2000). The lower signal-to-noise ratio is due to a thick specimen and a high particle concentration, and it can cause incorrect velocity calculations in PIV analysis. To increase the signal-to-noise ratio, the particle concentration should be decreased, but then a bigger interrogation volume, defined as the

[1]This is also called a "far-field" diffraction condition, which is defined as $R > a^2/\lambda$, where $R$ is the smaller of the two distances from the particle to the objective lens and the objective lens to the imaging detector, $a$ is the particle radius, and $\lambda$ is the wavelength in the medium. For typical conditions for micro-PIV, $R \sim 1$ mm, $a \sim 200$ nm, and $\lambda \sim 500$ nm, the inequality is well satisfied by a ratio of greater than 12,000.

[2]Numerical aperture, $NA$, is defined as $NA \equiv n_i \sin\theta_{max}$, where $n_i$ is the refractive index of the immersing medium (air, water, oil, etc.) adjacent to the objective lens, and $\theta_{max}$ is the half-angle of the maximum cone of the light apertured by the lens.

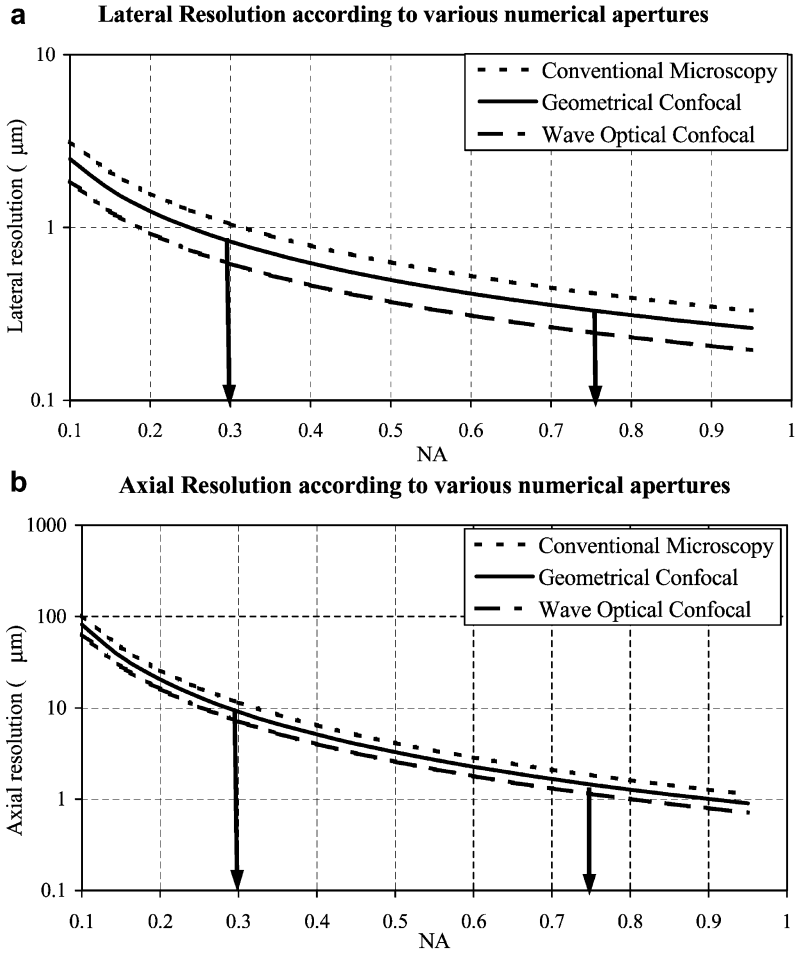


**Fig. 3a, b.** Calculated lateral resolution (**a**) and axial resolution (**b**) as functions of objective *NA* for $n$=1.0 (air), $\bar{\lambda}_{ex}$=488 nm, $\bar{\lambda}_{em}$=515 nm, and $\bar{\lambda} = 500.96$ nm. (The *arrows* indicate the *NA* conditions of the objectives used for the present experiment)

interrogation window multiplied by the effective DOF, is inevitably required to get the adequate number of particle pairs.

## 2.2 Confocal microscope

The pinhole diameter is an important parameter for confocal microscopy and plays a decisive role in determining its image resolutions. When the modified pinhole diameter[3], *PD*, is greater than one Airy unit (AU[4]), i.e., *PD*>1.0 AU, a geometric-optical analysis is used, whilst for *PD*<0.25 AU, a wave-optical analysis is applied (Wilhelm et al. 2003). Summarized results are also presented in Table 1 for the lateral/axial resolution formulae for both geometric-optical and wave-optical confocal microscope systems. The lateral resolution uses a criterion based on full-width at half-maximum (FWHM) of two neighboring PSF images at the confocal plane, somewhat analogous to the Rayleigh criterion of a conventional microscope, but additionally accounting for the pinhole effect of spatial filtering on the image construction that is restricted from the full Airy pattern of Fraunhofer diffraction. Likewise, the axial resolution of a confocal microscope is based on the FWHM of PSF constructed along the optical axis.

The image resolution of confocal microscopy is generally determined by the multiplication of the PSF of the illuminating light source (the illuminating PSF) and the PSF of the emitted fluorescent light (the emitting PSF), as schematically illustrated in Fig. 1a. For wave-optical confocal microscopy with sufficiently small *PD*, the FWHM of the illuminating PSF and that of the emitting PSF are comparable in their magnitudes, and both PSFs are needed to determine the total PSF imaged on the recording plane. Therefore, both lateral and axial resolutions of the wave-optical confocal microscope are specified by the functions of the mean wavelength, $\bar{\lambda}$[5], of $\lambda_{em}$ and $\lambda_{ex}$. On the other hand, for the geometric-optical confocal microscope with relatively larger *PD*, the FWHM of the emitting PSF is larger than that of the illuminating PSF and the deterministic resolutions can be specified solely by the smaller PSF, i.e., the illuminating PSF. Consequently, both the lateral and axial resolutions of the geometric-optical confocal microscope are specified by functions of only the excitation wavelength, $\lambda_{ex}$. Note that the image resolutions of conventional microscopy depend only on the emission wavelength $\lambda_{em}$.

Figure 3 shows the calculated resolution dependency on *NA* for both regular and confocal microscopes under

[3]Modified pinhole diameter, *PD*, is defined as *pinhole diameter/magnification*, with the pinhole diameter measured in μm.

[4]Airy unit, AU $\equiv 1.22\lambda_{ex}/NA$, with $\lambda_{ex}$ being the fluorescent excitation wavelength.

[5]The mean wavelength is defined as, $\bar{\lambda} = \sqrt{2}\frac{\lambda_{ex}\cdot\lambda_{em}}{\sqrt{\lambda_{ex}^2+\lambda_{em}^2}}$.

typical fluorescence excitation ($\lambda_{ex}$=488 nm) and emission ($\lambda_{em}$=515 nm) bands in the air. As anticipated, confocal microscopy resolutions are consistently better than regular microscopy, and both lateral and axial resolutions decrease significantly with increasing *NA*. The arrows indicate the conditions of the objectives used for the present study: 10× with 0.3*NA* and 40× with 0.75*NA*; both fall in the geometric-optical confocal range as shown in Table 2. Note that the nominal magnifications are specified for the conventional microscopic imaging, but they had to be corrected for the case of the confocal microscopy since the optical paths are routed through the confocal unit before the detector, resulting in slightly reduced actual magnifications. While the lateral resolution of the confocal microscope is slightly better than that of the conventional microscope, the confocal axial resolution shows more than 20% improvement from the conventional microscope.

A more exclusive and unique feature of confocal microscopy may be represented by its optical slicing capability. Since, in practice, the focused region is defined approximately as a "lobe" elongated along the optical axis, rather than as an ideal point, primarily because of spherical and/or chromatic aberrations, it constitutes a distributed probe imaging volume laterally as well as axially (Fig. 4). For a conventional microscope, when the imaging plane moves away from the focal plane, the image focusing degrades but the integrated amount of the emitted light energy remains more or less unchanged, as long as the defocusing distance is smaller than the axial dimension of the probe volume. As a result, off-focused images are blurred and larger in size with reduced intensity (reduced number of photons received per unit area), but their total number of photons remain more or less the same due to having no spatial filtering restrictions. Since the entire flow field is illuminated in the line-of-sight direction in the micro-PIV configuration, the integrated and blurred images contribute to degrading the measured velocity vector fields. The effective depth, so-called the depth-of-correlation, over which particles contribute to the measured velocity has been well documented elsewhere in the case of conventional micro-PIV measurements (Thiery et al. 1996; Prenel and Bailly 1998; Olsen and Adrian 2000).



In contrast, for the case of spatial filtering by a pinhole of confocal microscopy, the maximum number of photons is recorded only when the focal plane (image plane a in Fig. 4) is imaged because of the minimal level of spatial filtering imposed by the pinhole. As the defocusing level progresses with image planes, b, c, and d, the integrated light energy drops dramatically since the level of the spatial filtering increases progressively with the degree of defocusing. This allows true "optically sliced" image recording for confocal microscopy. No such definition for optical slicing is possible for conventional microscopy. Therefore, the confocal microscope can exclusively observe fluorescence particles near the focus, with a peak of the integrated light energy, and the detected light energy falls off sharply as one moves out of focus, as schematically illustrated in Fig. 4.

Analytical expressions for the optical slice thicknesses that were developed theoretically with experimental corrections from multiple contributors (Kimura and Munakata 1990; Qian and Elson 1991; Sandison and Webb 1994; Webb 1996; Born and Wolf 1999; Diaspro 2002; Wilhelm et al. 2003; http://www.solameretech.com; http://www.microscopy.fsu.edu; http://www.health.auckland.ac.nz/biru/confocal_microscopy) are tabulated for both geometric-optical and wave-optical ranges in Table 1. Note that the slice thickness for the geometric-optical

**Table 2.** Representative optical parameters for the present study

| | | |
|---|---|---|
| $\lambda_{ex}$, excitation wavelength (μm) | 0.488 | |
| $\lambda_{em}$, emission wavelength (μm) | 0.515 | |
| $\bar{\lambda}$, mean wavelength (μm) | 0.500879 | |
| Refraction index | 1.0 | |
| *NA* | 0.75 | 0.3 |
| Overall magnification | 40 (37.6) | 10 (9.4) |
| Airy unit (AU) | 0.793 | 1.984 |
| Pinhole diameter (μm) | 50 | 50 |
| *PD* (μm) | 1.329 | 5.319 |

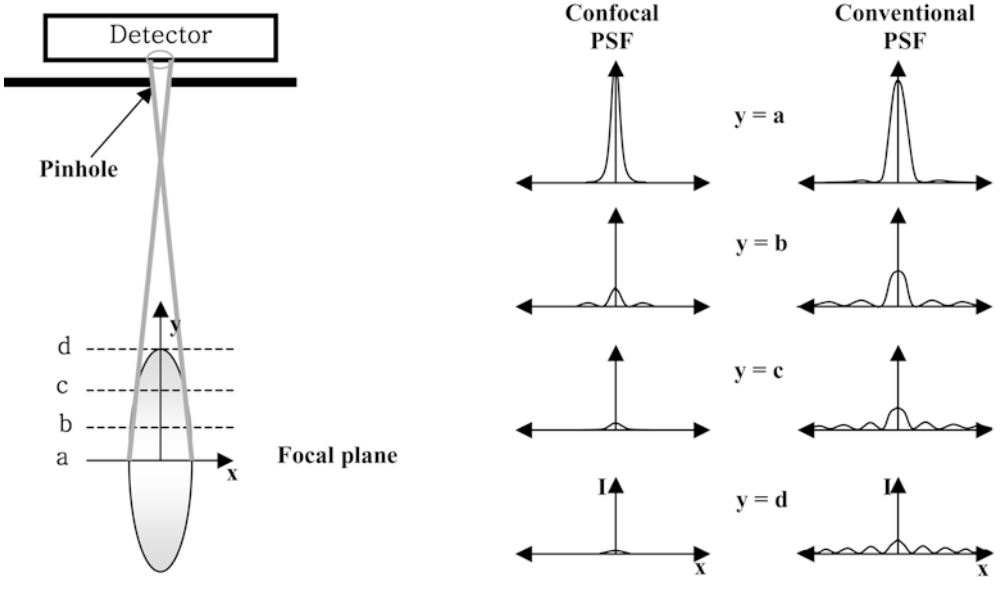


**Fig. 4.** A schematic illustration of the extended imaging probe around the ideal focal plane and the image intensity patterns (so-called point spread function, PSF) projected onto the detector plane from the focal plane (*a*) and from off-focal planes (*b*, *c*, and *d*)

range depends on the pinhole diameter, whereas for the wave-optical range, a single formula is defined uniquely for all pinhole diameters, as long as they satisfy the criterion of $PD<0.25$AU, which implies the cases of sufficiently small pinhole diameters. Figure 5a presents the dependence on *NA* of the calculated optical slice thickness of a geometric-optical confocal microscope for different pinhole diameters ranging from 30 μm to 150 μm in air ($n$=1.0 and$\lambda_{em}$=515 nm) for a specified magnification of 37.6×. The optical slice thickness substantially decreases with increasing *NA* and with reduced pinhole diameters. The arrow shows the calculated slice thickness of 2.820 μm for the 40×-0.75*NA* objective lens used for the present experiment. Figure 5b shows the calculated optical slice thickness of a wave-optical confocal microscope, corresponding to an ideal case of a pinhole diameter tending to zero, or infinitesimally small, for three different media, consisting of air ($n$=1.0), water ($n$=1.33), and silica glass or a special oil environment ($n$=1.516), for the case of $\bar{\lambda} = 500.96$ nm. The use of a water or oil immersion environment increases the corresponding *NA*and the resulting optical slice thickness will be significantly reduced from that in the air environment. The arrows indicate the optical slice thicknesses corresponding to the *NA* values of 0.3 and 0.75, as examples, should these objective lenses fall in the wave-optical category, i.e., for the case when using with extremely small pinhole diameters.

Tables 2 and 3 show optical parameters for the present experimental consideration for typical cases and the calculated optical resolutions and optical slice thicknesses using the formula presented in Table 1. The confocal microscope system at the Micro/nano-scale Fluidics and Heat Transport Laboratory of Texas A&M University http://go.to/microlab falls under the geometric-optical confocal microscope as both $PD$=1.329 for the 40× nominal (37.6× confocal) magnification and $PD$=5.319 for the 10× nominal (9.4× confocal) magnification are larger than the corresponding unit AU values of 0.793 and 1.984, respectively. The objective lenses are semi-apochromatic and of air-immersion types. The optical slice thickness is estimated to be less than 3 μm for the 40×-0.75*NA* objective and less than 27 μm for the 10×-0.3*NA* objective. Note that, since most of the optical considerations for confocal microscopy have been made for relatively higher *NA* values, the derived formula may not accurately predict the slice thickness for the 10×-0.3*NA* case and, as a result, the estimation of 27 μm may well be overestimated.



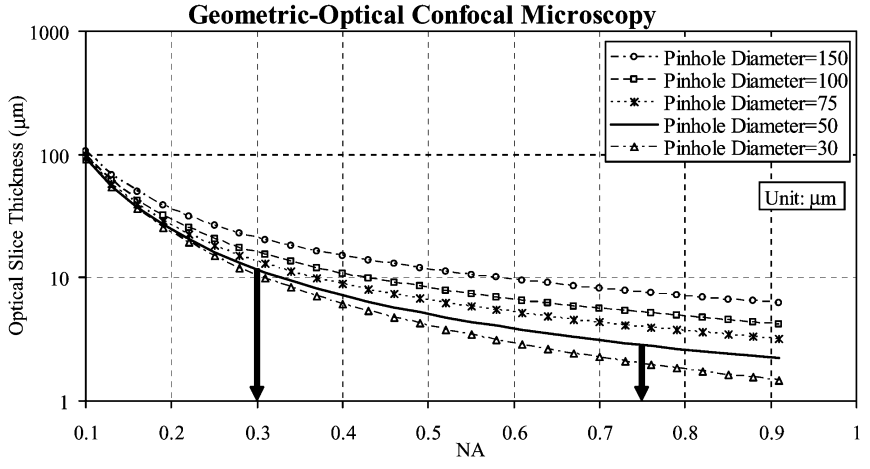


**(a) $n$ = 1.0, $\lambda_{em}$ = 515 nm, 40X Nominal, 37.6X Confocal magnifications**

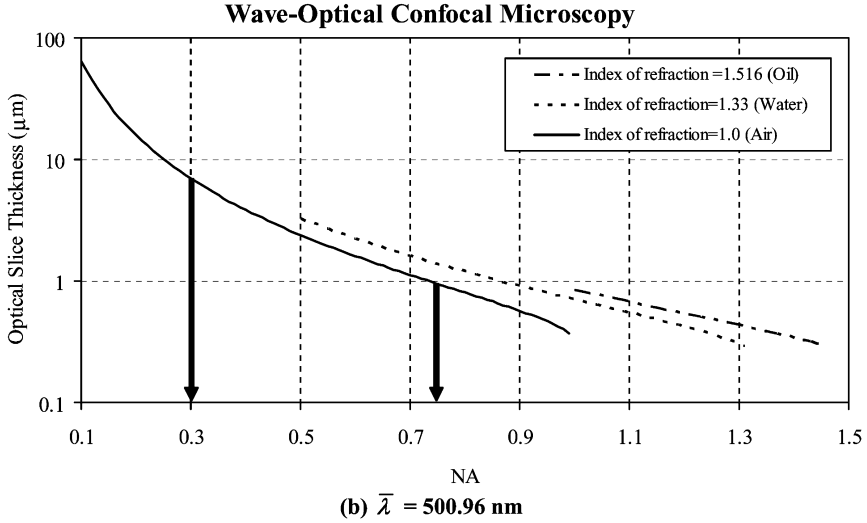


**(b) $\bar{\lambda}$ = 500.96 nm**

**Fig. 5a, b.** Calculated optical slice thickness for a geometric-optical confocal microscope (**a**) and for a wave-optical confocal microscope (**b**). (The *arrows* indicate the *NA* conditions of the objectives used for the present experiment)

**Table 3.** The optical resolutions and slice thickness of the confocal microscope system at the Micro/nano-scale Fluidics and Heat Transport Laboratory of Texas A&M University (http://go.to/microlab)

| | Conventional microscope | | Geometric-optical confocal microscope | | Wave-optical confocal microscope | |
|---|---|---|---|---|---|---|
| | 40× | 10× | 40× | 10× | 40× | 10× |
| Lateral resolution (μm) | 0.418 | 1.047 | 0.331 | 0.829 | 0.247 | 0.617 |
| Axial resolution (μm) | 1.831 | 11.444 | 1.268 | 9.323 | 0.946 | 6.959 |
| Optical slice thickness (μm) | Not defined | | 2.820 | 26.701 | 0.946 | 6.959 |



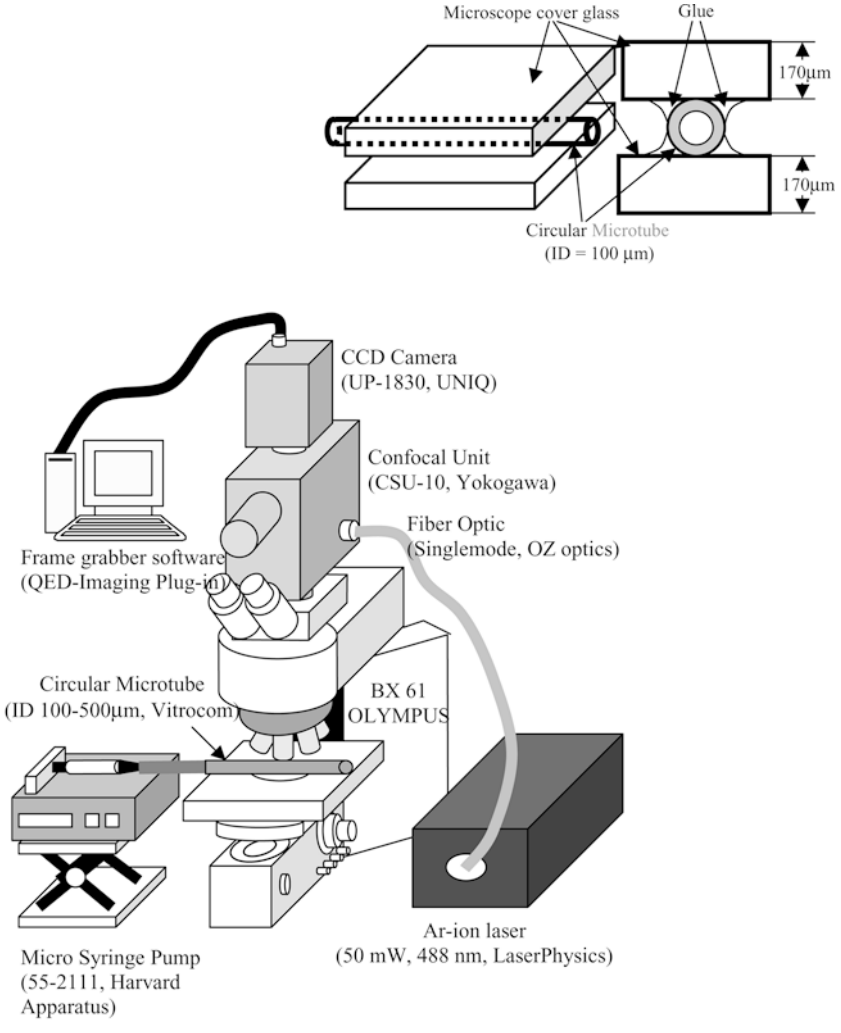


**Fig. 6.** Test setup of a micro-Poiseuille flow experiment

## 3 Experimental setup and PIV analysis

### 3.1 Experimental setup

The experimental setup (Fig. 6) consists of a dual-Nipkow disk confocal module (CSU-10, Yokogawa, Japan), an upright microscope (BX-61, Olympus, Japan), a 50-mW CW argon-ion laser (tuned at 488 nm, Laser Physics, U.S.A.), a frame grabber board (QED Imaging, USA), and PIV analysis software (DaVis, LaVision, Germany). The lower inlet port of the confocal head unit is attached to the ocular port of the microscope and the upper outlet port is connected to the CCD camera (QED Imaging UP-1830, UNIQ, 1024×1024 pixels at 30 FPS). The tested microtubes are laid between the two 170-μm-thick standard cover slip glasses, and all three are bonded together using clear instant cyanolite based glue, so-called "Super Glue" as a product name in USA. Seeding particles used for the PIV experiment are yellow-green (excited at 505-nm band peak and emitting at 515-nm band peak) fluorescent microsphere beads of 200-nm-diameter and 1.05 specific gravity (Molecular Probes Inc.).

The tested microtube is made with Borosilicate glass and one end is connected to a micro-syringe by Teflon tubing. Two different syringes pumped by a micro-pump generate constant flow rates of 30 μl/hr and 0.75 μl/hr, which are applied for 500-μm and 100-μm microtubes,

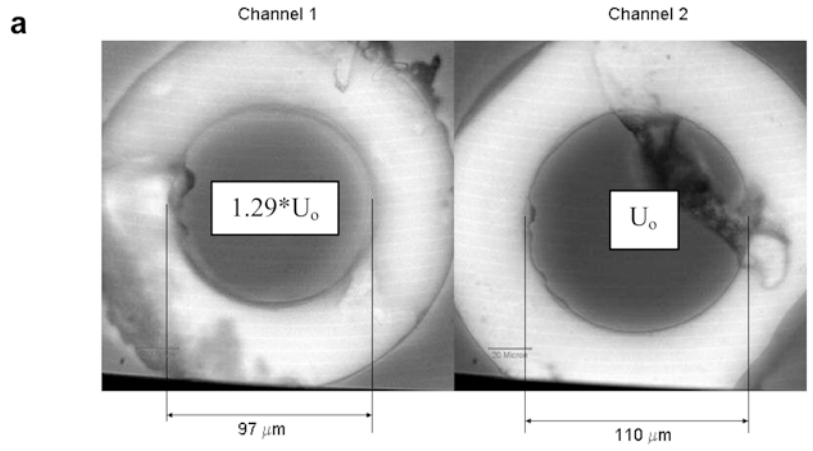


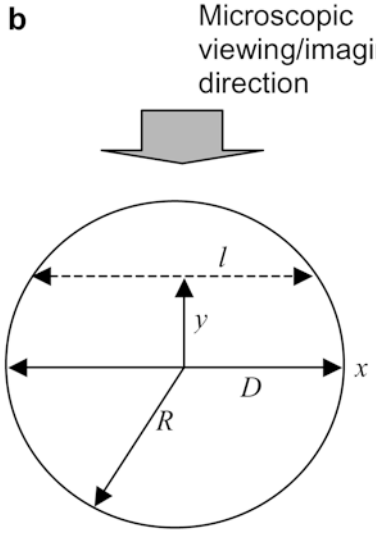


| *y/R* | *l/D* |
|---|---|
| **0** | **1.0** |
| 0.2 | 0.980 |
| 0.4 | 0.917 |
| **0.6** | **0.800** |
| 0.8 | 0.600 |
| **0.9** | **0.436** |
| 0.95 | 0.312 |
| **0.98** | **0.198** |
| 1.0 | 0 |

**Fig. 7a, b.** Tested microtubes. **a** Actual-size variations of the two microtubes of the same 100-μm nominal inner diameter, ID. **b** True image size, *l*/*D*, as a function of the distance from the center plane, *y*/*R*

respectively. Their corresponding Reynolds numbers are 0.00275 and 0021, respectively, based on the average flow velocity and the tube diameter. The cross-sections of tested microtubes were imaged by a microscope to accurately measure their actual diameters (Fig. 7). For example, two different microtubes with the same nominal 100-μm ID demonstrate actual diameter variation of over 13% and average velocity differentials of about 24%. The image plane width, *l*, decreases from the microtube diameter, *D*, at the center plane, *y*=0, to zero at *y*=*R*. The microscopic stage micrometer identifies the top end plane, *y*/*R*=1, at which low-populated stationary particles are imaged, and then the stage is lowered by the amount corresponding to the measured microtube radius, *R*, divided by the medium refractive index[6] (in water, *n*=1.33) to locate the center at *y*/*R* = 0. Note that the division by the refractive index of water is necessary to compensate for the index mismatching created by the fluid filled inside the microtube. The spatial uncertainty of the imaging planes is conservatively estimated, i.e., using the larger uncertainty levels of the conventional microscope[7], to be ±1.04 μm for 40× and ±5.74 μm for 10× magnification.

### 3.2
### PIV analysis

The standard cross-correlation scheme based on FFT, developed by LaVision, Inc., was used to process the PIV

[6]The reduced apparent depth, $h_a$, is derived as *h*/*n*, based on Snell's law of refraction (Hecht 2002). Strictly speaking, the analysis assumes a planar interface and zero ray-incident angle, thus, for the case of a circular microtube, it is only valid along the centerline (refer to Fig. 9).

[7]The spatial uncertainty of the imaging planes is estimated as an rms of the one-half of the micro-stage reading resolution, 0.5 μm, and the uncertainty level for identifying the top-end point is estimated to be approximately identical to the image depth-of-field (DOF), 0.92 μm for 40× and 5.72 μm for 10× magnification, for the conventional microscope. Note that the values of DOF for CLSM are 0.63 μm and 4.66 μm for 40× and 10× magnification, respectively.

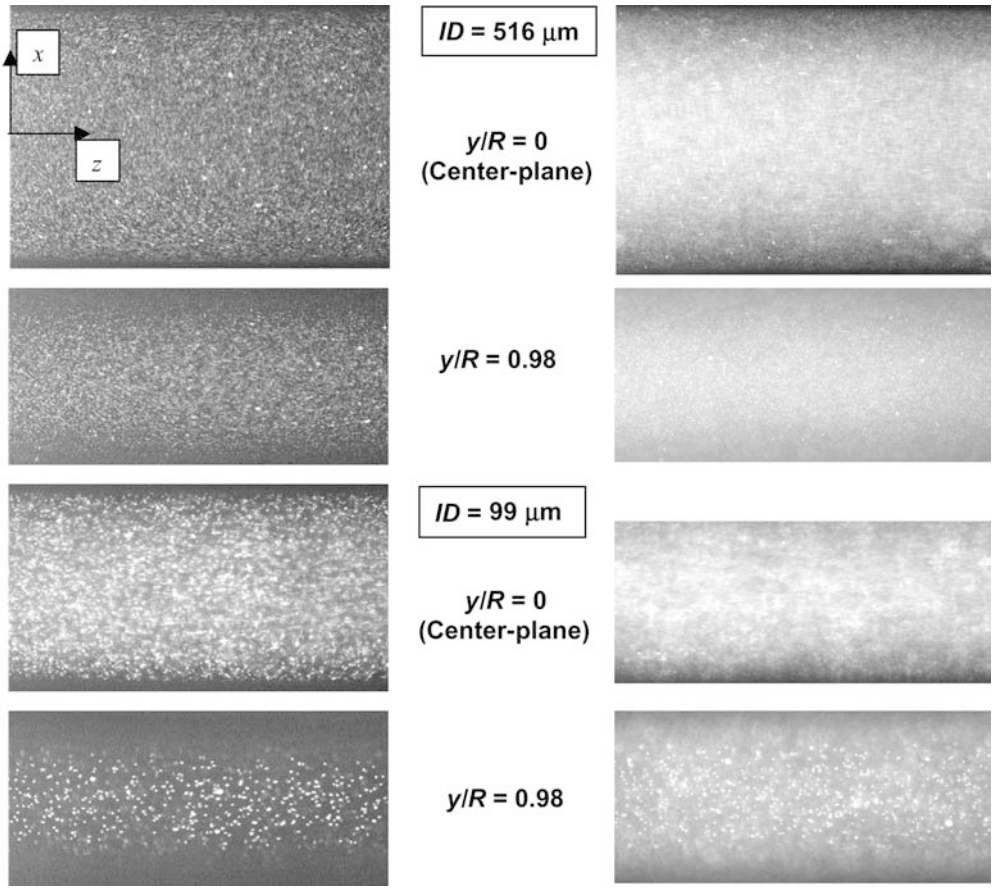


**Fig. 8**. Particle images taken at two different $y$ planes by CLSM (*left*), and by conventional epi-fluorescence (*right*) microscopy

images to obtain the raw vector field. The scheme implements a multi-pass interrogation process with an adaptive offset algorithm to enhance the signal-to-noise ratio. The first pass cross-correlation is calculated for a 64×64-pixel interrogation volume by FFT without volume offset, and then the interrogation volume is divided into four subareas of 32×32-pixel size for the second pass calculation. The estimated displacement value obtained from the first pass calculation is used as the volume offset value for the second pass calculation. The displacement values of the four highest cross-correlation peak locations, corresponding to the four interrogation volumes of the second pass calculation, are stored for presentation.

Cross-correlation between two successive image frames at 30 FPS results in an inter-frame time of 33 ms. As flow tracers, 200-nm fluorescent spheres are seeded at 0.01% in volume for the 99-μm microtube, and 0.002% for the 516-μm microtube, for best results based on the examination of particle images, ensuring that each interrogation volume consists of at least five pairs of well defined particle images. Each interrogation volume of 32×32 pixels corresponds to a 5.5-μm×5.5-μm area for the 99-μm microtube, and a 22-μm×22-μm area for the 516-μm microtube. Regarding the signal-to-noise ratio, the thick specimen results in lowering the signal-to-noise ratio, so the lower particle concentration is required to compensate for the lower ratio. Note that the diameter of microtube is increased by a factor of five whilst the particle concentration is reduced by five times.

## 4
## Results and discussion

### 4.1
### Comparison of particle images between conventional microscopy (epi-fluorescent) and confocal microscopy (CLSM)

In Fig. 8, the raw PIV images are shown for two selected planes of $y/R$=0 at the center plane, and $y/R$=0.98 near the top end of the microtube inner surface. The 516-μm ID microtube is imaged at 9.4× confocal or 10× conventional microscopy, and the 99-μm ID microtube, at 37.6× or 40×, respectively. The confocal microscopic images demonstrate optically sliced images with clear image definition of individual particles located within the slice thickness. On the contrary, the conventional microscopic images are largely obscured by the blurred, off-focus images[8], as the line-of-sight dimension of the microtube far exceeds the estimated DOF of 0.92 μm for 40×, or 5.72 μm for 10× magnification (Table 3). In addition, the stray light rays that are internally reflected from the microtube inner surface, and externally refracted/reflected rays through the curved microtube wall, enter the detector without being spatially filtered and cause further deterioration of the

[8]The background noise from the off-focus particle images can be reduced to an acceptable level by limiting the PIV measurement depth to a base-cut level where the field-wide-averaged image intensity reaches one-tenth of the maximum in-focus image intensity (Meinhart et al. 2000).

particle images. Although there are a number of techniques known to improve PIV images, including the use of an oil-immersion objective with high *NA*, or the use of a pulsed laser for illumination, no further attempt has been accommodated at present since the primary interest is to compare the image and velocity field data quality between CLSM micro-PIV and conventional micro-PIV under specified and identical imaging conditions.

The apparent image diameter[9] of 200-nm particles, when back-projected to the physical domain, is estimated to be 2.1 μm for 10× imaging of the 516-μm microtube, and 0.86 μm for 40× imaging of the 99-μm microtube, assuming that negligible particle image streaks occur from the particle displacement during a finite shutter opening time. The relative particle image size normalized by the tube diameter, i.e., 0.87% for the 99-μm microtube is more than two times bigger than 0.42% for the 516-μm microtube. In the case of the smaller microtube, the relatively larger image size makes it essential to accommodate the reduced particle number density because the seeding concentration is increased by only five times.



Another point to note is that the normalized flow velocity based on the microtube diameter for the smaller microtube ($0.545\ \mathrm{s}^{-1} \equiv 54\ \ \mu\mathrm{m}\cdot\mathrm{s}^{-1} \Big/ 99\ \ \mu\mathrm{m}$) is more than three times higher than that for the larger microtube ($0.154\ \mathrm{s}^{-1} \equiv 79.7\ \ \mu\mathrm{m}\cdot\mathrm{s}^{-1} \Big/ 516\ \ \mu\mathrm{m}$), and this explains the greater number of image streaks shown for the 99-μm microtube compared to the 516-μm microtube. The 54-μm/s flow velocity is bound by the lower limit of the volume flow rate of 0.75 μl/hr given by the micro-syringe pump used. The particle image streaks during the 33.3-ms exposure time at 30 FPS are 1.8 μm for the 99-μm microtube (more than two times larger than the particle image size of 0.86 μm or 33% of the 5.5-μm interrogation volume size) and 2.7 μm for the 516-μm microtube (approximately the same as the particle image size of 2.1 μm or 12.3% for the 22-μm interrogation volume size). Therefore, the resulting PIV flow vector field data for the smaller microtube will likely be subjected to more bias because of its lower particle image density and the higher normalized velocity.

To compensate for such bias, a more rigorous analysis for the PIV software improvement has been extensively studied using a highly accurate high-resolution PIV technique, particularly to improve the sub-pixel measurement accuracy (Sugii et al. 2002). At present, despite the fact that these aspects could be improved to an extent by carefully altering the related parameters for the PIV analysis, no further attempt has been contemplated since the comparative observation for the level of such bias is important to characterize the differences between conventional and CLSM micro-PIV systems. Another way to alleviate the image streaking bias will be to use a sufficiently short-pulsed illumination to freeze the imaging frame, which is commonly exercised by many researchers in using conventional micro-PIV (Santiago et al. 1998).

### 4.2
### Curved image planes compensating for the refractive index mismatching

The refractive index mismatching (Merzkirch 1987), between the tested flow (water, $n$=1.33 at $\lambda$=500 nm), the microtube wall (Borosilicate glass, $n$=1.475), the glue layer (Cyanoacrylate, $n\sim$1.33), the cover slip glass (Crown glass, $n$=1.544 at $\lambda$=515 nm, and $n$=1.547 at $\lambda$=488 nm), and the air ($n$=1.0) medium before the microscope objective, makes it necessary to compensate for correcting depths in association with the varying thickness ratios at different ray incidence locations (Fig. 9). Calculations were conducted to account for the optical path length differentials[10] by using the geometrical ray optics analysis with a first-degree approximation of zero-incident angles for all rays based on the paraxial imaging assumption, which is acceptable for the present objectives with relatively low *NA* used on a non-oil immersion basis. The analysis allows corrections for the actual imaging depths and determining the corrected curved image plane, as shown by the solid lines in the case of 99-μm ID microtube in Fig. 9. Although not shown repeatedly, the 516-μm ID microtube case showed similar, but relatively less pronounced corrections because of its relatively larger radius of curvature. The actual imaging points, along the vertical centerline only, match with the flat imaging plane and the deviation progressively increases with the radial distance from the center point.

The lens effect caused by the curved and thick microtube wall (approximately 35-μm-thick for the 99-μm ID microtube, and 101-μm-thick for the 516-μm ID microtube) makes an additional image correction necessary. Although a full version of the ray optical analysis is available for the lens effect corrections, a more comprehensive (presumably more accurate and integrative) experimental correction has been used by comparing the apparent image widths, as measured in Fig. 8, and the predicted image widths, as shown in Fig. 9. The lens effect of the microtube makes uncertainties in visually determining the wall locations inevitable, particularly when the image plane is approaching the center plane and the amount of refraction increases. By matching the two, the locations of individual PIV data points are corrected in a proportional way, from no correction at the center point to maximum correction for the last data point near the wall. The observation uncertainty of wall locations is estimated to be equal to the differential (either positive or negative) between the ideally calculated wall location based on the aforementioned curved plane analysis and the location of the outmost visible particles. The maximum uncertainties

[9]The actual recorded image of a seed particle on the CCD is a convolution of the geometric particle image, $Md_\mathrm{p}$, with the FPS, $d_\mathrm{s}$, of the recording optics. Approximating both of the geometric and diffraction-limited images as Gaussian functions, the image diameter, $d_\mathrm{e}$, can be expressed as (Born and Wolf 1999) $d_\mathrm{e} = \left[M^2 d_\mathrm{p}^2 + d_\mathrm{s}^2\right]^{1/2}$ where $d_\mathrm{e}$ is the effective particle diameter inthe CCD, $M$ is the magnification of the microscope, $d_\mathrm{p}$ is the particle diameter, and $d_\mathrm{s}$ is the characteristic diameter of the PSF. For magnifications much larger than unity, the diameter of the diffraction-limited PSF, in the image plane, is given by $d_\mathrm{S} = 2.44M\frac{\lambda}{2NA}$ where *NA* is the numerical aperture and $\lambda$ is the wavelength of light.

[10]Optical path length (OPL) is defined as the local medium thickness multiplied by the local refractive index.

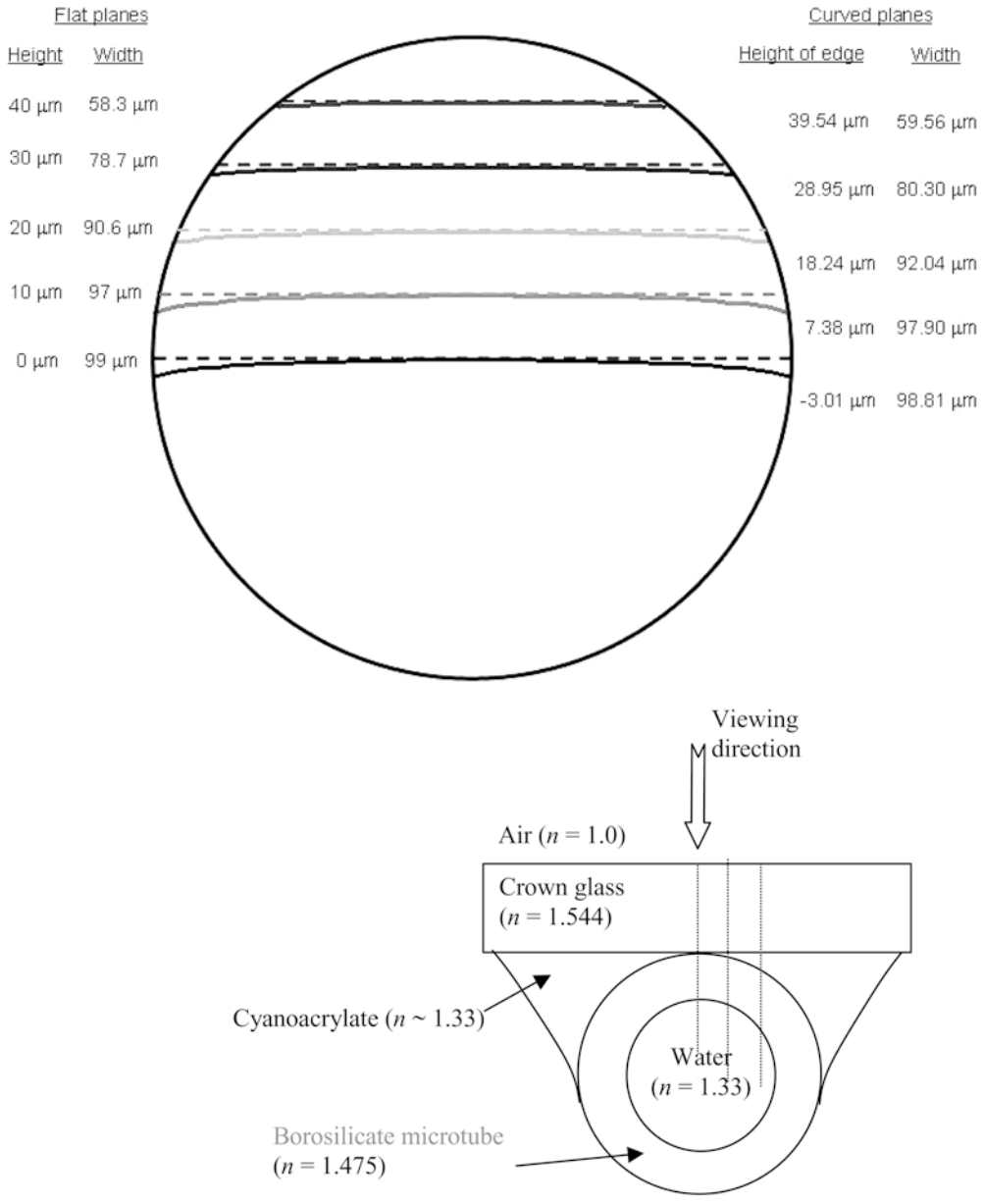


**Fig. 9.** Curved image planes (*solid lines*) corrected to compensate for the refractive index mismatching through the multiple layers and uncorrected flat image planes (*dashed lines*) for the 99-μm ID microtube. (Values of refractive indices for the multiple layers are evaluated for 500 nm<$\lambda$<515 nm.)

of the wall locations are estimated to be 2.4 μm for the 99-μm microtube and 12.6 μm for the 516-μm microtube.

### 4.3
### Poiseuille velocity profiles developed in microtubes

Figures 10 and 11 show measured velocity profiles at different $y$ planes of the 99-μm and 516-μm microtubes, respectively. The solid symbols represent the CLSM micro-PIV data, the regular symbols for the conventional micro-PIV data, and the parabolic curves represent the ideal Poiseuille flow profiles that are depth-corrected, accounting for the aforementioned refractive index mismatching.

All of the displayed results represent the flow field of raw vectors with no attempt for an artificial validation scheme to be implemented so that the imaging capabilities between the CLSM micro-PIV system and the conventional micro-PIV system are exclusively compared. The error bars represent 95% standard deviations of the averaged data of 30 axial locations at constant $x$ for each image and for all 29 PIV image pairs processed, i.e., the average of the 870 velocity profiles combined. Note that the Poiseuille flow profile is calculated directly from the specified volume flow rate conditions without attempting any normalization for the velocity profiles, i.e., 54-μm/s center maximum velocity from 0.75 μl/hr for the 99-μm microtube or 79.7-μm/s center maximum velocity from 30 μl/hr for the 516-μm microtube. The laminar flow entrance or developing length is given as $L/D$=0.65 (Lew and Fung 1970) and the corresponding length is calculated to be $L$=64.4 μm for the smaller microtube and $L$=335 μm for the larger. Thus, the tested microtube flows have a negligibly small entrance region to establish fully developed Poiseuille flow within less than a one-diameter distance from the entrance.

For the 99-μm microtube, the CLSM data at the center plane (Fig. 10a) shows a fairly good agreement with the calculated Poiseuille profile as anticipated by the exactly resolved depth-wise PIV imaging by the well defined optical slice thickness of 2.82 μm (Table 3), whereas the

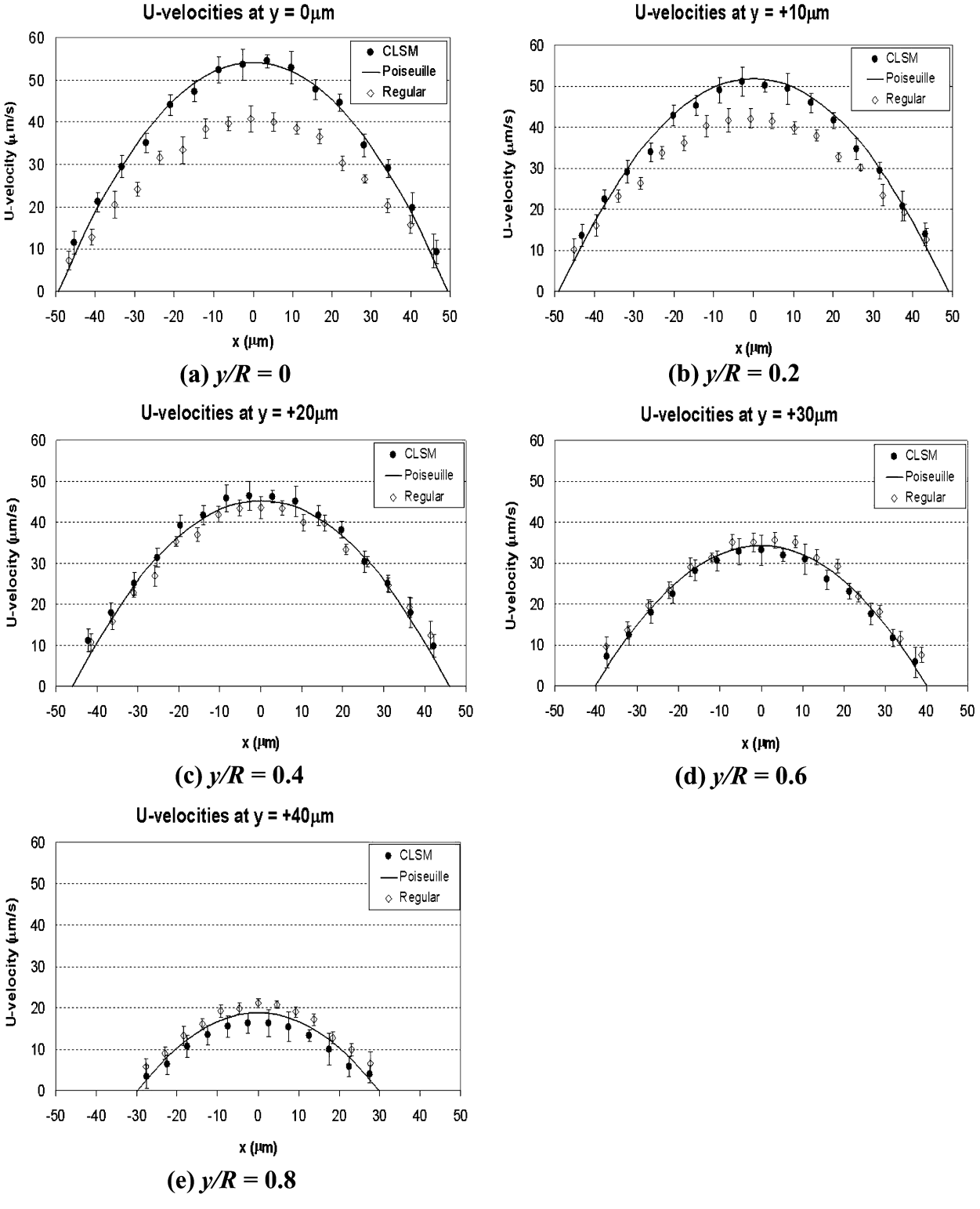


**Fig. 10.** Comparison of the velocity profiles measured by CLSM micro-PIV and by conventional micro-PIV at different $y$ planes of the 99-μm ID microtube

conventional micro-PIV data shows substantial underestimation of −13.3 μm/s from the calculations. We believe that the primary reason for such large discrepancies is attributed to the lack of the optical slicing capability of conventional microscopy, and the particular reason for the underestimation is due to the negative bias caused by the out-of-focus foreground as well as background blurred images that are moving slower than the fastest center plane flow movement. The centerline velocity biases ($x$=0) at other planes of $y/R$=0.2, 0.4, 0.6, and 0.8, are measured to −9.7 μm/s, −1.7 μm/s, +1.4 μm/s, and +2.3 μm/s, respectively. The magnitude of the negative

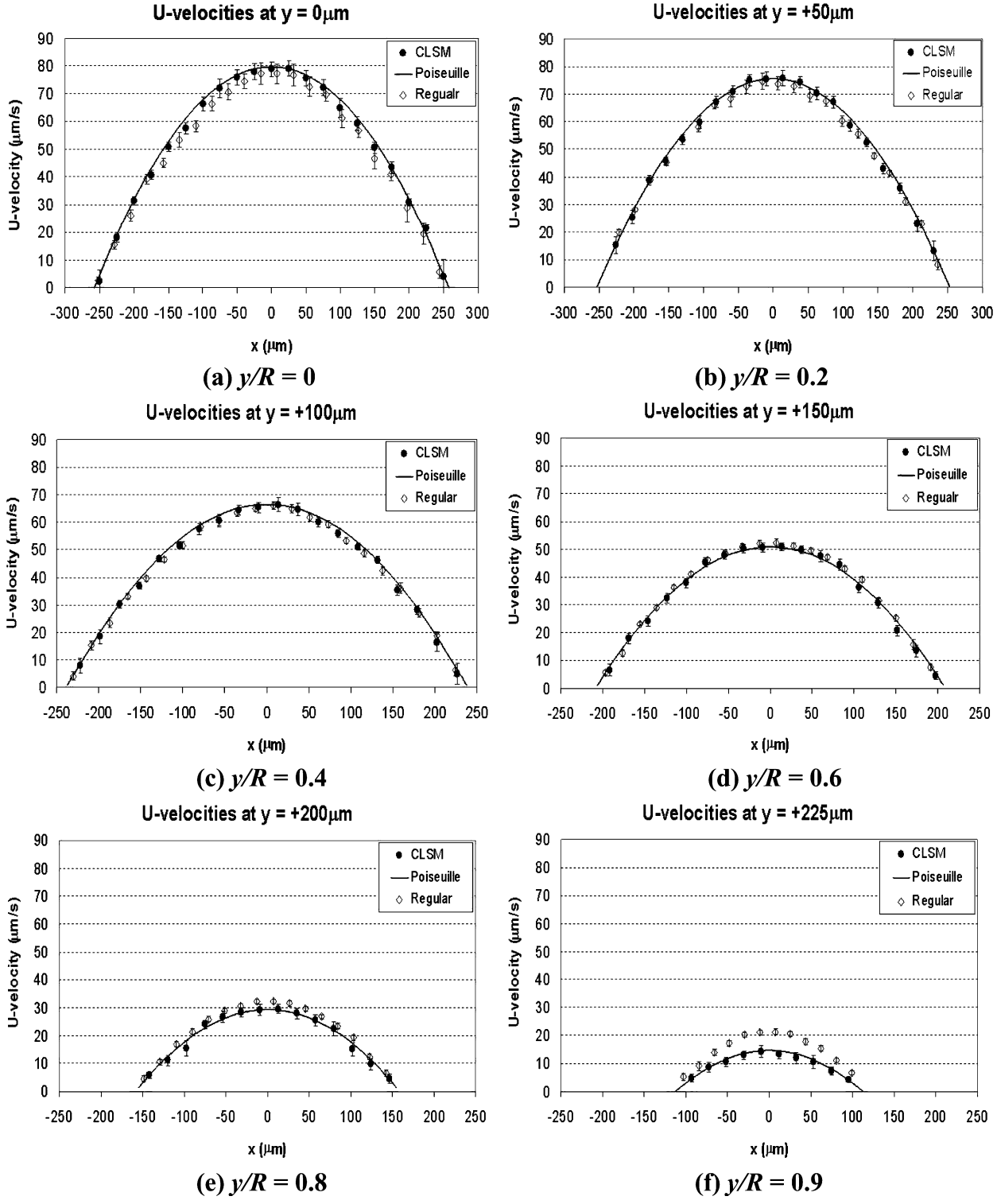


**Fig. 11.** Comparison of the velocity profiles measured by CLSM micro-PIV and by conventional micro-PIV at different $y$ planes of the 516-μm ID microtube

bias gradually diminishes away from the center plane to $y/R$=0.2 (Fig. 10b), and becomes minimal at $y/R$=0.4 (Fig. 10c) as a balance is supposedly reached between the positive bias imposed by the faster background flow near the center plane region ($y/R$<0.4), and the negative bias due to the slower foreground flow near the microtube edge region ($y/R$>0.4).

Further away from the center plane, at $y/R$=0.6 and 0.8 (Fig. 10d and e), a transition from the negative bias to the positive bias is observed, and this is believed to be the fact that, as the top inner microtube wall is approached, the positive bias by the faster moving background flow in the region of $y/R$<0.8 becomes dominant and the negative bias is diminished by the significantly reduced microtube edge

region of $y/R>0.8$. In contrast, the CLSM-PIV data remain in fairly well agreement with the calculated profiles at all of the tested $y$ planes. The last CLSM profile shown in Fig. 10e, measured only 10 μm away from the microtube edge, starts showing some perceivable degree of deviations. This is possibly due to the more drastic velocity magnitude changes near the wall; even within such a thin optical slice thickness of 2.82 μm, the velocity gradient becomes steeper as the microtube wall is approached. An additional reason for the enlarged deviations may be attributed to the more substantial lens effect and internal reflection occurrence due to the relatively thick lens for the relatively narrow flow region.



For the 516-μm ID microtube, the magnitudes of the negative bias for the conventional PIV results near the center plane (Fig. 11a and b) are dramatically reduced in comparison with the previous 99-μm microtube case. As shown in Fig. 8, and discussed previously, the PIV image quality for both the CLSM and the conventional cases is noticeably improved for the larger microtube with the lower magnification (10× nominal), and the advantageous feature of CLSM micro-PIV is less pronounced for the objective with low numerical aperture ($NA$=0.3) used for its imaging. At $y/R$=0.4 and 0.6 (Fig. 11c and d), both the CLSM-data and the conventional PIV data agree well with the theory showing negligible bias. At larger $y/R\geq0.8$ (Fig. 11e and f), however, the positive biasing starts to appear and the bias progressively grows with increasing $y/R$, while the CLSM results stay in fairly close agreement with the theoretical Poiseuille profiles. As the microtube wall is approached, the PIV image quality degradation is amplified because of the dramatically increased lens effect distorting images and the severe image obscuration caused by the internal reflection. Consequently, the bias of the conventional micro-PIV is amplified whereas the CLSM micro-PIV results more or less consistently show good agreement. This indicates that the optical slicing works more effectively to improve the data accuracy when the PIV image quality is not optimized. Note that the CLSM imaging in general shows more distinctive improvement with higher magnifications and with higher $NA$ objectives, and should be even more pronounced with oil-immersion-based objectives with $NA$ larger than unity.

## 5 Conclusive remarks

Confocal laser scanning microscopy (CLSM) is applied to a micro-scale flow field measurement by means of particle image velocimetry (PIV), and its images and results are compared with those of conventional epi-fluorescence microscopy. The dual Nipkow disk of Yokogawa, CSU-10, is noticeably beneficial to measure micro-scale flow fields because of its high-speed frame rates of up to 120 FPS, as well as the unique optical slice capability by its confocal spatial filtering. A novel design to increase the Nipkow disk scanning rate will be crucial to apply the CLSM micro-PIV technique for future micro-fluidic applications with higher velocity ranges.

The optical path length compensation with regard to the refractive index mismatching of different mediums in the line-of-sight direction is properly discussed to correct the actual depths and determine the optically distorted curved imaging planes. Furthermore, the actual locations of PIV data points are corrected for the lens effect occurring from the curvature of the microtube wall.

Carefully measured PIV data for micro-scale Poiseuille flows for the two different microtubes of 99-μm and 516-μm diameter show that the CLSM micro-PIV results agree well with the theoretical profiles, mainly because of the optical slicing.The conventional micro-PIV results are substantially deviating due to the lack of the optical slicing capability and the bias resulting from the out-of-focus blurred images and low contrast of particle image intensities. The distinction of CLSM micro-PIV for its improved measurement accuracy is more pronounced for the case of the smaller microtube with high magnification and high $NA$ imaging objective.

## References


Born M, Wolf E (1999) Principles of optics, 7th edn. Cambridge University Press, Cambridge, UK, pp 491

Conchello JA, Lichtman JW (1994) Theoretical analysis of a rotating-disk partially confocal scanning microscope. Appl Opt 33:585–596

Diaspro A (ed) (2002) Confocal and two-photon microscopy: Foundations, application, and advances. Wiley-Liss, New York, pp 101–125, 245–247

Egner A, Andersen V, Hell SW (2002) Comparison of the axial resolution of practical Nipkow-disk confocal fluorescence microscopy with that of multifocal multiphoton microscopy: Theory and experiment. J Microsc 206:24–32

Hecht E (2002) Optics, 4th edn. Addison Wesley, Reading, MA, pp 467–471

Hell S, Reiner G, Cremer C, Stelzer EHK (1993) Aberrations in confocal fluorescence microscopy induced by mismatches in refractive index. J Microsc 169:391–405

Ichihara A, Tanaami T, Isozaki K, Sugiyama Y, Kosugi Y, Mikuriya K, Abe M, Uemura I (1996) High-speed confocal fluorescence microscopy using a Nipkow scanner with microlenses for 3-D imaging of single fluorescent molecule in real time. Bioimaging 4:57–62

Kimura S, Munakata C (1990) Depth resolution of the fluorescent confocal scanning optical microscope. Appl Opt 29:489–494

Lew HS, Fung YC (1970) Entry flow into blood vessels at arbitrary Reynolds number. J Biomech 3:23–28

Meinhart CD, Wereley ST, Gray MHB (2000) Volume illumination for two-dimensional particle image velocimetry. Meas Sci Technol 11:809–814

Merzkirch W (1987) Flow visualization, 2nd edn. Academic Press, Orlando

Minsky M (1998) Memoir on inventing the confocal scanning microscope. Scanning 10:128–138

Olsen MG, Adrian RJ (2000) Out-of-focus effects on particle image visibility and correlation in microscopic particle image Velocimetry. Exp Fluids 29:S166-S174

Prenel JP, Bailly Y (1998) Theoretical determination of light distributions in various laser light sheets for flow visualization. J Flow Vis Image Proc 5:211–224

Qian H, Elson EL (1991) Analysis of confocal laser-microscope optics for 3-D fluorescence correlation spectroscopy. Appl Opt 30:1185–1195

Raffel M, Willert CE, Kompenhans J (1998) Particle image velocimetry: A practical guide. Springer, Berlin Heidelberg New York

Sandison DR, Webb WW (1994) Background rejection and signal-to-noise optimization in confocal and alternative fluorescence microscopes. Appl Opt 33:603–615

Santiago JG, Wereley ST, Meinhart CD, Beebe DJ, Adrian RJ (1998) A particle image velocimetry system for microfluidics. Exp Fluids 25:316–319

Sheppard CJR, Gu M (1991) Aberration compensation in confocal microscopy. Appl Opt 30:3563–3568
Sugii Y, Nishio S, Okamoto K (2002) In vivo PIV measurement of red blood cell velocity field in microvessels considering mesentery motion. Physiol Meas 23:403–416
Thiery L, Prenel JP, Porcar R (1996) Theoretical and experimental intensity analysis of laser sheets for flow visualization. Opt Commun 123:801–809
Tiziani HJ, Uhde HM (1994) Three-dimensional analysis by a microlens-array confocal arrangement. Appl Opt 33:567–572
Webb RH (1996) Confocal optical microscopy. Rep Prog Phys 59:427–471
Wilhelm S, Grobler B, Gluch M, Heinz H (2003) Confocal laser scanning microscopy: Principles. Carl Zeiss, pp 7–16